Electrochimica Acta 263 (2018) 261–271

Contents lists available at ScienceDirect

Electrochimica Acta

journal homepage: www.elsevier.com/locate/electacta

Electrocatalytic ammonia oxidation over a nickel foam electrode: Role of $Ni(OH)_{2(s)}$-$NiOOH_{(s)}$ nanocatalysts

Yu-Jen Shih [a], Yao-Hui Huang [b], C.P. Huang [c, *]

[a] Institute of Environmental Engineering, National Sun Yat-sen University, Kaohsiung, 804, Taiwan, ROC
[b] Department of Chemical Engineering, National Cheng-Kung University, Tainan, 701, Taiwan, ROC
[c] Department of Civil and Environmental Engineering, University of Delaware, Newark, DE, 19716, USA

ARTICLE INFO

Article history:
Received 31 October 2017
Received in revised form
29 December 2017
Accepted 8 January 2018
Available online 10 January 2018

Keywords:
Electrode kinetics
Nano-$NiOOH_{(s)}$-$Ni(OH)_{2(s)}$
Nitrogen selectivity
Ammonia oxidation

ABSTRACT

Direct electrocatalytic oxidation of ammonia was carried out using an open-pore structured nickel foam electrode via electrochemical formation of $Ni(OH)_2$/NiOOH nano-flowers (theophrastite phase) on the nickel substrate at specific overpotentials. The electrode surface was analyzed by X-ray diffraction (XRD), scanning electron microscope (SEM), Raman spectrometer (RS), and X-ray photoelectron spectroscopy (XPS). Cyclic voltammograms gave information on the nature of electron transfer between nitrogen species and nickel foam electrode and revealed the potential dependence nature of ammonia oxidation over the potential window of +0.7 V to +0.85 V (vs. Hg/HgO). Batch controlled potential experiments using nickel foam as the working anode in a three-electrode system were conducted to study the oxidation of ammonia in solution containing 0.1 M of Na_2SO_4 electrolyte, at pH 11 and temperature of 25 °C. Based on the current efficiency and reaction kinetics, it was possible to establish the mechanism of selective ammonia conversion to gaseous nitrogen and nitrate.

1. Introduction

Nitrogen cycle consists multiple steps of biologically mediated transformation of nitrogenous species, which control the availability of nutrients and subsequently affect the primary productivity of aquatic systems [1]. Inorganic nitrogen in forms of nitrate, nitrite, and ammonium are commonly available for microbial assimilation. Nitrate, readily bio-assimilable after sequentially reduced to nitrite and ammonium, is a nitrogen species commonly preferred by phytoplanktons [2]. Excessive nutrients, including phosphates, carbon, and nitrogen, may result in algal blooms (eutrophication) in freshwater as well as marine environments. Wastewater discharge from human activities, including agriculture, landfill, pharmacy, dyeing and photoelectric industries impacts the aquatic nitrogen cycle, thereby prompts the Urban Waste Water Directive (92/271/EEC) of the European Water Framework Directive (2000/60/EC) call for a discharge limit of 10 ppm-N in ecologically sensitive areas [3].

Breakpoint of chlorination or electrochlorination can eliminate ammonia from wastewaters by controlling the distribution between free chlorine and ammonia and pH [4]. However, chlorine-based chemicals potentially react with ammonia nitrogen to form chloramines and halogenated byproducts, which are highly toxic toward humans. Anammox™ is a microbially mediated process by which the bacterial phylum *Planctomycetes* directly convert nitrite and ammonium to nitrogen gas [5]. Although Anammox™ is effective in treating ammonium-rich wastewaters, it requires large land space and long process time compared to chemical methods, such as electrochemical ammonia oxidation [6,7]. Early interest in ammonia oxidation was focused on improving the process efficiency of selective catalysis reduction (SCR) units in minimizing ammonia slip. There were extensive studies on the oxidation of ammonia by oxygen in gas phase over metallic catalysts, namely, Pt, Rh, and Pd [8] and metal oxides such as CuO/TiO_2 [9], NiO/Al_2O_3 [10,11], CuO/Al_2O_3 [12–14] and CuO/Fe_2O_3 [15–18]. High percent nitrogen selectivity was achievable at temperature in the range of 200–300 °C. There are many studies on ammonia fuel cells using single-crystal Pt or Pt-based alloys as electrodes [19–22]. By contrast, there is little systematic study on electrochemical ammonia oxidation for the control of nitrogen nutrients in natural water, especially using low-cost and effective electrodes synthesized from non-noble metal oxides.

---

* Corresponding author.
E-mail address: huang@udel.edu (C.P. Huang).

https://doi.org/10.1016/j.electacta.2018.01.045

Metallic nickel is widely used in rechargeable alkaline batteries (Ni/Cd, Ni/H_2, Ni/Zn) and supercapacitors [23,24]. Eq. (1) shows the oxidation of Ni(0) to yield nickel hydroxide, $Ni(OH)_2$, at a specific pH and free electron activity, i.e. pe. (Fig. S1 shows the distribution of Ni species at oxidation state of 0, II, III, and IV as a function of pH-pε.).

$$Ni(OH)_{2(s)} + 2e^- = Ni(0) + OH^-;\ E^0 = -0.215\ \text{V (vs. NHE)} \quad (1)$$

Further oxidation of $Ni(OH)_2(s)$ yields nickel oxyhydroxide, $NiOOH_{(s)}$, a black-colored compound as shown in Eq. (2),

$$NiOOH(s) + e^- + H_2O \overset{\text{charging}}{\leftarrow} Ni(OH)_{2(s)} + OH^-;\ E^0 = 0.49\ \text{V (vs. NHE)} \quad (2)$$

In the last decade studies on the ammonia oxidation over $Ni(OH)_2$/NiOOH electrode was focused on the preparation of $Ni(OH)_2$ thin films for energy applications [25–28]. To the best of our knowledge, there is little investigation on the feasibility of Ni metal supported NiOOH film for the electrochemical treatment of ammonia containing wastewaters. The aim of this work was to study the oxidation of ammonia toward nitrogen selectivity in alkaline solutions over nickel foam electrode. The distribution of intermediate nitrogen species, ammonia removal efficiency and nitrogen selectivity were assessed under constant potential. Cyclic voltammetry was used to determine the reaction steps and number of electron transferred at the electrode-water interface. The electrode surface, namely, nickel oxides, was characterized in the absence and presence of NH_3 by X-ray diffraction (XRD), scanning electron microscope (SEM), Raman spectroscopy (RM), and X-ray photoelectron spectrometer (XPS).

2. Material and method

2.1. Chemicals

The ammonia solution was prepared by dissolving a given amount of ammonium sulfate, $(NH_4)_2SO_4$ (J.T. Baker, USA), in a given volume of deionized water. The supporting electrolyte was prepared by sodium sulfate (Na_2SO_4, Sigma-Aldrich Co., USA), conditioned to a specific pH using sodium hydroxide (NaOH, Merck KGaA, Germany) and sulfuric acid (H_2SO_4, 95%, Sigma-Aldrich Co., USA). Chemicals for the analysis of electrochemical intermediates including sodium nitrite ($NaNO_2$), sodium hypochlorite (NaClO), *N*-(1-Naphthyl) ethylenediamine dihydrochloride ($C_{10}H_7NHCH_2CH_2NH_2 \cdot 2HCl$), sulfanilamide ($H_2NC_6H_4SO_2NH_2$), and sodium phenoxide ($NaOC_6H_5 \cdot 3H_2O$) were purchased from Sigma-Aldrich Co., USA; potassium nitrate (KNO_3) and sodium nitroprusside ($Na_2[Fe(CN)_5NO]$) were purchased from Riedel-deHaën AG, Germany; ethylenediaminetetraacetic acid disodium salt dihydrate ($C_{10}H_{14}N_2Na_2O_8 \cdot 2H_2O$, EDTA-$Na_2$) was purchased from U&I Bio-Tech, Inc., USA. All reagents were of analytical grade and used without further purification. The deionized water purified with a laboratory-grade RO-ultrapure water system (resistivity >18.18 MΩ cm) was used to prepare all solutions.

2.2. Experimental procedure

Electrochemical cells were powered by a potentostat (CHI611C, CH Instruments, Inc., USA). The working electrode was a nickel foam (thickness = 2 mm, area density ~ 250 g m^{-2}, mesh = 94 ± 10, Innovation Materials Co., Ltd., Taiwan). The counter electrode was an iridium oxide-coated titanium (Ti/IrO_2) plate, cut into the same dimension as the working electrode; the reference electrode was Hg/HgO/1 M NaOH ($E^0 = 0.14$ V vs. NHE) (RE-61AP, ALS Co. Ltd., JAPAN). The voltammetric response was recorded by sweeping over a specific potential range at specific rate (ν, V s^{-1}). Prior to experiments, the nickel foam was degreased with acetone (99.5%), acid-etched in 3 M of H_2SO_4 for 10 min and then rinsed with deionized water in an ultrasonic bath. Batch ammonia oxidation (20 ppm NH_3-N) experiments were conducted under constant potential (amperometry) mode at pH 11 and 25 °C. The dimension (submerged in electrolyte) of the nickel anode, cylinder in shape, was 3 cm in diameter and 3.5 cm in length. A cahode, Ti/IrO_2 cylinder with 1 cm in diameter and 3.5 cm in length was placed concentrically inside r of the cylindrical anode, yielding an average electrode-to-electrode spacing of 1 cm (the configuration of electrochemical cell is provided in Fig. S2).

2.3. Chemical analysis

A flow injection analyzer (FIA, Lachat's Quik Chem 8500 Series 2, USA) was used to analyzing the concentration of aqueous nitrogen species (NH_3-N, NO_3^--N, NO_2^--N). Ammonia was analyzed by the indophenol method (at 630 nm) based on the Berthelot reaction, a catalytic reaction among phenolate, hypochlorite, and ammonia, with nitroprusside as the catalyst [29]. The total oxidized nitrogen (NO_x) was determined by reducing nitrate to nitrite (in a copperized cadmium column) prior to a diazotization of nitrite with sulfanilamide followed by coupling with *N*-(1-naphthyl)-ethylenediamine dihydrochloride (NED). Concentration of the pink azo dye produced was then calibrated spectrophotometrically at 540 nm [30] against standard solutions. Nitrate concentration was the difference between total NO_x and nitrite, which was determined separately. The limit of detection was 0.2 μg/L for NH_3-N, and 0.25 μg/L for NO_2^--N and NO_3^--N.

The chemical state of the nickel foam electrode was examined by X-ray photoelectron spectroscopy (XPS, PHI 5000 VersaProbe, PHYSICAL ELECTRONICS, INC., USA) with a monochromatic Al Kα X-ray source (1487 eV). A scanning electron microscopy (SEM, JSM-6700F, JEOL Ltd., Japan) was used to observe the micromorphology of the nickel foam electrode. The crystallographic structure was analyzed by X-ray diffraction (XRD, DX III, Rigaku Co., Japan) operated with Cu Kα source ($\lambda = 1.5406$ Å) at a scan rate of 0.06°/s in the incidence angle range of 20–85° (2θ). Raman spectra were obtained using a DXR™ microscope (Thermo Fisher Scientific Inc., USA).

3. Results and discussion

3.1. Electrochemical analysis of nickel foam in the presence of ammonia

Fig. 1 shows the polarization curves (log i - E) in the potential range where metallic nickel oxidation (corrosion) and $Ni(OH)_2$/NiOOH transformation occurred. The Tafel slope was computed from the log I versus E (CV) curve (i.e., potentiodynamic method) at scan rate of 0.5 mV/s (geometric area = 1 × 2.5 cm^2, $[Na_2SO_4] = 0.1$ M as supporting electrolyte). This electrolyte concentration is able to maintain constant conductivity necessary for operating the whole electrode system while minimizing other side effects, such as redox reaction of background electrolyte species and gas evolution, i.e., O_2 at anode and H_2 at cathode. The sulfate ion is inert to participating at other faradaic reactions, such as cathodic deoxygenation ($E^0 = -0.4$ V) [31] under the selected analytical potential range, which is mainly for the chemical oxidation of ammonia. We have reported the

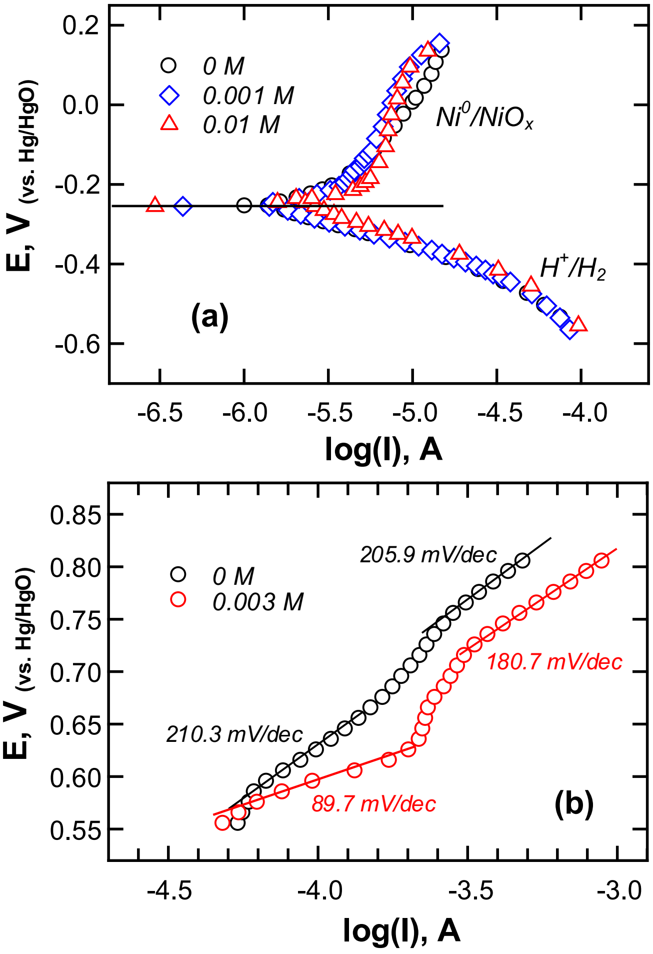

Fig. 1. Dependence of log *i*-E curves on ammonia concentration (nickel foam electrode = 1 × 2.5 cm^2, 0.1 M Na_2SO_4, pH 11) at potential ranges for (a) metallic corrosion and hydrogen evolution and (b) formation of nickel hydroxide and oxyhydroxide.

formation of oxide layer on metallic nickel surface at pH > 9.0 previously [32]. Since the acidity constant of NH_4^+/NH_3 equilibrium is $10^{-9.25}$, a pH of 11 was selected for studying the electrocatalytic oxidation of ammonia. The electrochemical oxidization (or corrosion) of nickel metal typically followed the following half reactions [33],

For anodic oxide film formation:

$$Ni(0) + 2xOH^- \rightarrow NiO_{x(s)} + xH_2O + 2xe^- \ (0 < x < 1) \quad (4)$$

For cathodic hydrogen evolution:

$$2H_2O + 2e^- \rightarrow H_{2(g)} + 2OH^- \quad (5)$$

As shown in Fig. 1a, the open circuit potential (i.e., E^0) was *ca.* −260 mV and the Tafel plots were not affected by the presence of ammonia (at 10^{-3} and 10^{-2} M). Obviously, ammonia did not participate at any electrochemical reactions in the potential range studied when the oxidation of Ni to nickel oxide occurred. On the other hand, Ni foam exhibited two identical Tafel slopes of 205.9 and 210.3 mV/dec at +0.58 and +0.73 V, respectively (Fig. 1b), which could be attributed to the formation of oxyhydroxide phases [34]. The polymorphisms of α- and β- $Ni(OH)_{2(s)}$ were transformed to γ-$NiOOH_{(s)}$ and β-$NiOOH_{(s)}$, respectively. Furthermore, β-$NiOOH_{(s)}$ was transformed to γ-$NiOOH_{(s)}$ when the electrode was overcharged (Bode cycle) [35]. According to Nernst equation, $E = E^0 + 0.059 \times pOH - E_{(Hg/HgO)}$ ($E_{(Hg/HgO)} = 0.14$ V at 0.1 M NaOH, the equilibrium potential of nickel hydroxide reduction to oxyhydroxide would be 527 mV at pH 11), which was close to the experimental value of 580 mV, indicating an overpotential of 53 mV. In the presence of 3 mM of ammonia, the Tafel slope for the formation of oxyhydroxide was 89.7 mV/dec. It was noted that the Tafel b value (b = 2.303/(1-α)nf) in the presence of ammonia was about half that of without ammonia, which implied that the number of electron involved in oxyhydroxide formation was doubled in the presence of ammonia.

Fig. 2 shows the CV curves obtained by sweeping at −0.5 V to a positive range of +0.4 V to +1.2 V. In the absence of ammonia (Fig. 2a), the faradaic reaction, peak O_1, occurred at the onset potential of +0.65 V, which was corresponding to a reversible reduction peak R_1. Gradually increasing the upper-potential limit to the onset of peak O_2 (+0.85 V) brought a R_2 shoulder. The O_1/R_1 and O_2/R_2 reversible reactions was due to the polarization of γ- and β-$NiOOH_{(s)}$. The total charge for α-$Ni(OH)_{2(s)}$ to γ-$NiOOH_{(s)}$ was higher than that of β-$Ni(OH)_{2(s)}$ to β-$NiOOH_{(s)}$. Furthermore α-$Ni(OH)_{2(s)}$ had better electrochemical reversibility than β-$Ni(OH)_{2(s)}$, per the smaller difference between E_{O1} and E_{R1}

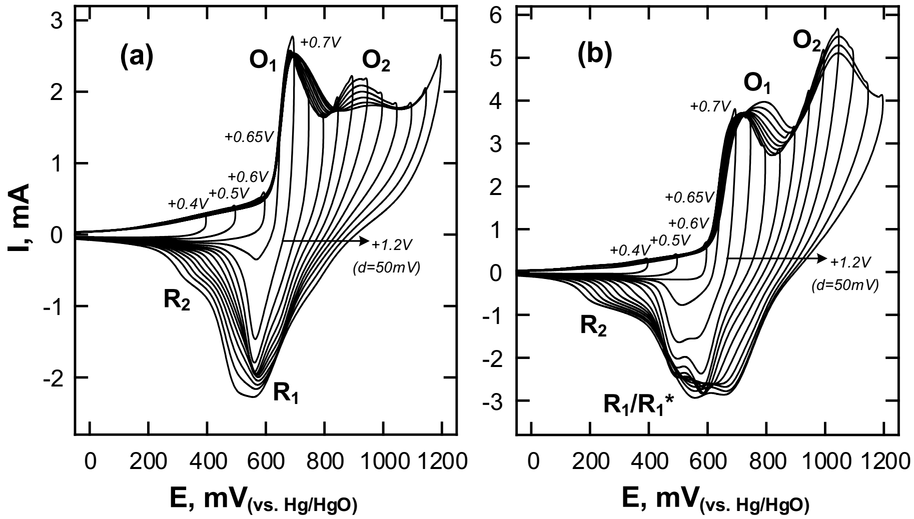

Fig. 2. Cyclic voltammograms recorded at Ni foam (1 × 2.5 cm^2) electrode in the presence of (a) 0 M and (b) 0.003 M ammonia using an inert electrolyte of 0.1 M Na_2SO_4 (pH 11). CVs differ by the upper-potential limit, started from −0.5 V to +0.4~+1.2 V (potential interval = 50 mV, scan rate = 10 mV-s^{-1}).

[36]. Based on results in Fig. 2a, it is possible to establish the following phase transition reactions:

$$\begin{tikzcd}
Ni^0 \arrow[r, "> -0.26\ V"] & NiO_x \arrow[r] & \alpha\text{-}Ni(OH)_2 \arrow[r] \arrow[d, shift right, "O_1"'] & \beta\text{-}Ni(OH)_2 \arrow[d, shift right, "O_2"'] \\
 & & \gamma\text{-}NiOOH \arrow[u, shift right, "R_1"'] & \beta\text{-}NiOOH \arrow[u, shift right, "R_2"'] \arrow[l, "(overcharge)"']
\end{tikzcd} \tag{6}$$

With the addition of 3 mM of ammonia (Fig. 2b), the current at peak O_1 and O_2 increased significantly. An additional R_1* peak appeared, that is, a split from R_1, when the potential was negatively scanned, which indicated the presence of a different reducible species overlapping with oxyhydroxide when the upper-potential was elevated to +0.7 V. In other words, the first electron transfer step between Ni foam and ammonia was chemically reversible, and the increment in current at peaks O_1 and O_2 was attributable to direct oxidation of ammonia-nitrogen.

Fig. 3 shows the CV-curve of the Ni foam electrode in the absence and presence of 3 mM of NH_3, in 0.1 M of Na_2SO_4 electrolyte at pH 11. A remarkable shoulder in the range of +0.3 to +0.6 V appeared, attributing to the charging of the double-layer capacitance of nickel hydroxide [37]. The double-layer charging occurs regardless of if the potential is sufficient to induce faradaic reactions or not; whereas highly porous electrode materials such as activated carbon [38] strongly magnify the double-layer capacitance. However, in the present work, the charging current exhibited by the nickel foam electrode below +0.6 V vs. Hg/HgO (without any redox reaction) is small, <60 μA (Fig. 1b). Therefore, nickel foam electrode can be considered a material with a low

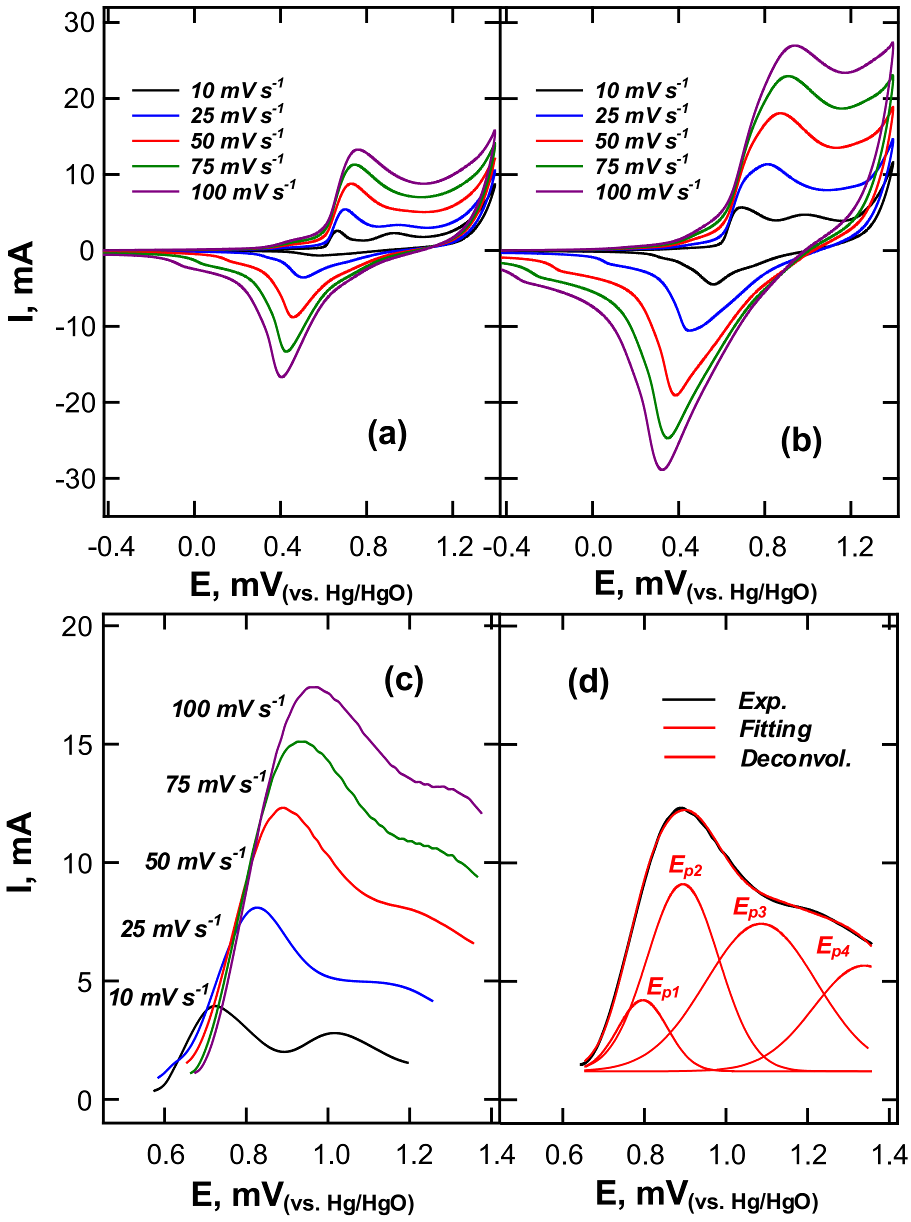

Fig. 3. Voltammograms for the Ni foam electrode (1 × 2.5 cm^2) within electrolytes (pH 11) of (a) 0.1 M Na_2SO_4 and (b) 0.1 M Na_2SO_4 + 0.003 M NH_3, recorded at scan rates from 10 to 100 mV-s^{-1}. (c) Net currents of NH_3 oxidation obtained by subtracting CVs free of NH_3 from that in 0.003 M NH_3. (d) Deconvolution of NH_3 current profile and the fitting result (50 mV-s^{-1}).

double-layer capacitance. When the potential increased to above +0.65 V, peak currents at O_1 and O_2 were increased with the scan rate. In inert electrolyte (Fig. 3a), the electrochemical process of a nickel hydroxide electrode has proven to be limited by solid-state intercalation through the lattice, thus diminishing the concentration polarization of proton during charge/discharge [39]. According to the Nicholson and Shain equation and based on peak current, I_p, as a function of scan rate, ν, the diffusivity coefficient of proton in the hydroxide film of the Ni foam electrode was calculated to be 5.52×10^{-12} cm^2-s^{-1}, which was comparable with those of powder-type nickel hydroxide electrodes reported in the literature [40,41]. Relevant variables related to O_1 peak in Fig. 3a were listed in Fig. S3. The peaks corresponding to $Ni(OH)_{2(s)}$ oxidation and $NiOOH_{(s)}$ reduction were broadened upon the addition of 3 mM of NH_3 (Fig. 3b). The corresponding E_p values were much pronouncedly shifted from low to high ν. Results suggested a decrease in the reversibility of the nickel hydroxide mediated nitrogen redox couples and consecutive multistep charge transfers occurring over the electrical double layer at the vicinity of the electrode [42]. Subtracting the corresponding result of Fig. 3a from Fig. 3b gives the net current for the redox reaction of NH_3 and intermediate nitrogen species as a function of ν (Fig. 3c). Results in Fig. 3c were used to analyze the multiple anodic processes by deconvolution of current profile in the potential window of +0.7 to +1.4 V using an Origin Pro. Software. Results in Fig. 3d show that the nickel electrode scanned at 50 mV/s had four distinct anodic peaks at 0.796, 0.895, 1.087, and 1.34 V, respectively. Voltammetric experiments were then conducted at different ammonia concentrations as at different sweeping rates. Apparently, the current at potential scanned larger than +0.6 V can be mainly attributed to ammonia oxidation since the faradaic current is a function of ammonia concentration as shown in Fig. S4; capacitance current contributed from Ni foam substrate is negligible, which also has been observed by Chen et al. [43]. Fig. 4a shows the αn_α value of the four peaks as a function of sweeping rate at different NH_3 concentrations. Results indicated that the E_p value was in the following deceasing order: $E_{p1} > E_{p2} > E_{p4} \sim E_{p3}$. This implied that ammonia oxidation occurred initially in two fast steps followed by two slow steps. That is, intermediates in each of the four-electron transfers had larger oxidation number (i.e., more oxidative) as the anodic potential was increased. In addition, the moderately scattered αn_α values indicated that the peak shape would vary with ν and ammonia concentration. (Fig. S5 shows details of the deconvoluted peaks.). Fig. 4b gives the plot of I_p versus $(\nu \times \alpha n_\alpha)^{1/2}$, which slope was concentration-dependent according to the Nicholson and Shain relation (Fig. 4c). Table 1 shows that the electron number transferred at E_{p1}, E_{p2}, E_{p3}, and E_{p4} was *ca.* 1, 3, 2, and 2, respectively (based on the average geometric area, A, of around 3.5 cm^2); that is, approximately a total of eight electrons were transferred in the complete oxidation of ammonia when voltage sweeping (at pH 11) was up to +1.4 V.

Based on the above results, it is possible to propose a general scheme for ammonia oxidation with stepwise dehydrogenation, which electrocatalytically generated NH_x, and ultimately surface atomic nitrogen species, $N_{2(ads)}$ [44], that is,

$$NH_{3(aq)} = NH_{3(ads)} \text{ (adsorption of aqueous ammonia)} \quad (7)$$

$$NH_{3(ads)} + OH^- \rightarrow NH_{x(ads)} + H_2O + (3-x)e^- \text{ (oxidation of adsorbed ammonia to ammonia hydrides)} \quad (8)$$

The recombination of surface NH_x species formed *N*-N bond*i.e.* bimolecular nitrogen species such as hydrazine, was the primary step to evolve N_2.

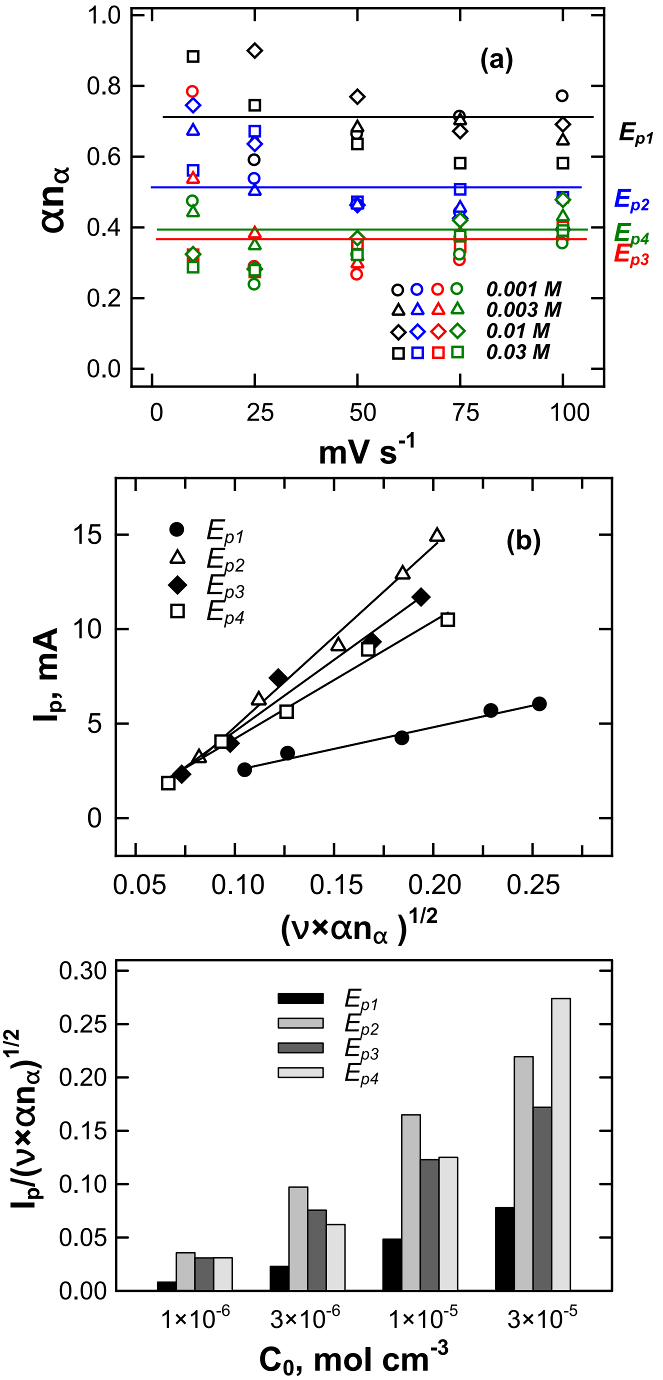

Fig. 4. (a) Effect of NH_3 concentration on the transfer coefficient as a function of scan rate. (b) Simple linear regression of peak currents vs. $(\nu \times \alpha n_\alpha)^{1/2}$ ($[NH_3] = 0.003$ M). (c) Slopes of peak currents vs. $(\nu \times \alpha n_\alpha)^{1/2}$ for peak potentials of E_{p1} to E_{p4} from various ammonia concentrations.

$$NH_{2(ads)} + NH_{x(ads)} \rightarrow N_2H_{y(ads)} \ (x = 1, 2, y = 3, 4) \quad (9)$$

$$N_2H_{y(ads)} + yOH^- \rightarrow N_{2(ads)} + yH_2O + ye^- \quad (10)$$

At low overpotentials, the first electron from E_{p1} may be assigned to the dehydrogenation of NH_3 (Eq. (8)), followed by the instantaneous recombination of $NH_{x(ads)}$ and the second step of electrons transfer from E_{p2} (Eq. (10)). On the other hand, a side reaction from oxidation of adsorbed $NH_{2(ads)}$ may yield $N_{(ads)}$:

Table 1
Electrochemical variables computed from anodic currents in the presence of ammonia.

	E_{p1}	E_{p2}	E_{p3}	E_{p4}
[a]E_p, mV	796	895	1087	1340
[b]αn_α	0.7	0.5	0.38	0.4
[c]m	4259	13144	9325	10075
n	1	3.1	2.2	2.3

[a] Data from CV in 3 mM NH_3 swept at 50 mV/s.
[b] Average values of transfer coefficient.
[c] Slope of $I_p/(v \times \alpha n_\alpha)^{1/2}$ against C_0 in Fig. 4c.

$$NH_{2(ads)} + 2OH^- \rightarrow N_{(ads)} + 2H_2O + 2e^- \quad (11)$$

Thus, E_{p2} was seen as a single peak with a peak current between that of N_2 (Eq. (10)) and $N_{(ads)}$ (Eq. (11)), further oxidation of $N_{(ads)}$ to NO_x occurred from E_{p3} onwards. At higher overpotentials, NO_x oxidized to nitrite and nitrate in alkaline solution [45]. As a whole, the electrochemical oxidation of ammonia over Ni foam electrode took place from *ca.* 0.6–0.8 V vs. Hg/HgO leading to the formation of a monolayer of NH_x as the key precursor of N_2. The selectivity gradually shifted toward the oxidation of the incipient $N_{(ads)}$ and nitro-oxides at potential > 0.8 V vs. Hg/HgO.

3.2. *Electrode characterization with respect to electrocatalytic ammonia oxidation*

Fig. 5a shows SEM micrograph of the blank Ni foam with vivid 3D open pores, mainly of pentagonal shape and 50–250 μm in size. Under higher magnification, the interconnected structures have a smooth surface before any treatment. The morphology of Ni foam electrode significantly was altered after 100 cycles of CV scans in the range of −0.5 to +1.2 V (50 mV-s^{-1}, 0.1 M Na_2SO_4 at pH 11); the rougher surfaces and edges (Fig. 5b), visualized as black spots on the electrode, were made of numerous nano-flowers (Fig. 5c). Fig. S7 shows results of repeating CV scans as to demonstrate the stability of the nickel foam electrode. Obviously, the shape of redox profile of Ni hydroxide is not altered, at least in 100 cycles. As a matter of fact, the current gradually improves with extended scan cycle because of the increase in the thickness of oxide film. The length of the coated nano-flowers was *ca.* 50–100 nm. Fig. 5d presents XRD patterns of Ni foam before and after electrochemical treatment. Ni foam exhibited a pure metallic nickel with diffraction peaks of (111), (200), and (220) planes at 2*θ* of 44.8°, 52.2°, and 76.8°, respectively. After CV scanning, the surface coated oxide film on the electrode was mostly a typical β-$Ni(OH)_{2(s)}$ mixed with minor signals of NiO(s)/$NiOOH_{(s)}$ phases. As shown in Fig. 6, Raman spectra of Ni foam sample revealed two peaks at *ca.* 50 and 612 cm^{-1} after repeating cycles of scanning from +0.2 to +0.6 V, which was correlated with Ni-OH and Ni-O stretching vibrations,

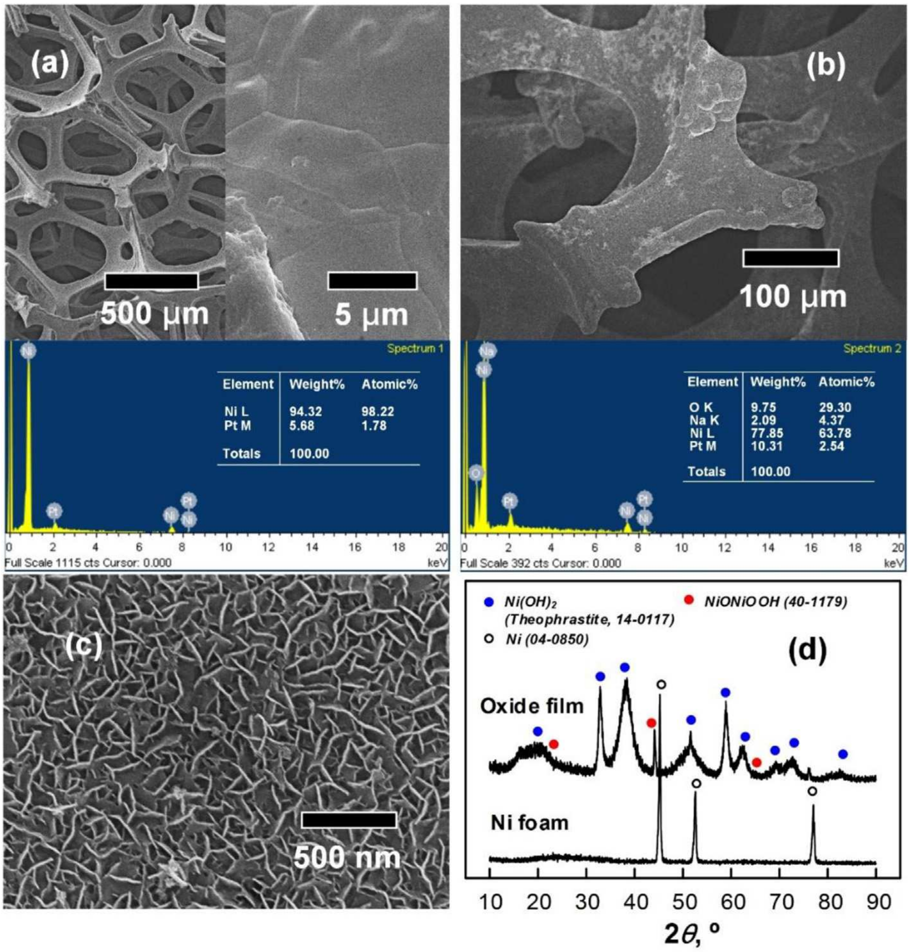

Element	Weight%	Atomic%
Ni L	94.32	98.22
Pt M	5.68	1.78
Totals	100.00	

Element	Weight%	Atomic%
O K	9.75	29.30
Na K	2.09	4.37
Ni L	77.85	63.78
Pt M	10.31	2.54
Totals	100.00	

Fig. 5. SEM images of Ni foam (a) before and after CV scanning at −0.5 to +1.2 V (vs. Hg/HgO) for 100 cycles at magnifications of (b) 250× and (c) 30,000×. (d) XRD patterns of Ni foam, and that with electrochemical treatment.

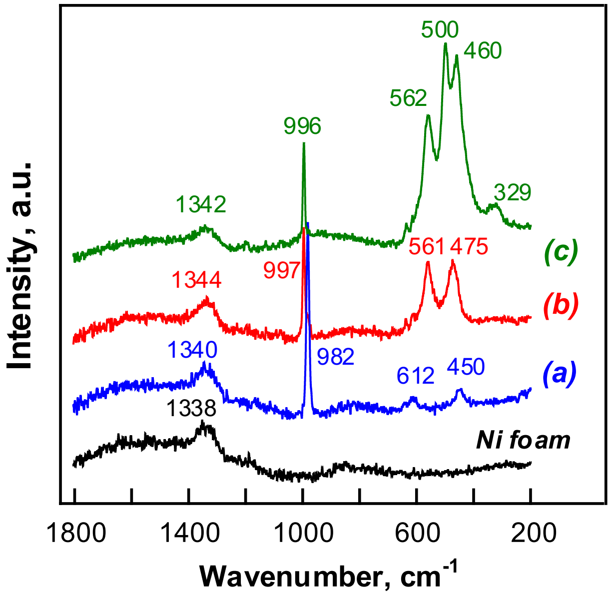

sample	disorder lattice	νNi-OH	νNi-O	vacancy defect
Ni	--	--	--	--
(a)	--	450	612	982
(b)	--	475	561	997
(c)	329	460	500/562	996

Fig. 6. Raman spectra of Ni foam electrode before and after CV scanning for 100 cycles in ranges of (a) +0.2 V to +0.6 V and +0.4 V to +0.8 V in the (b) absence and (c) presence of 0.01 M NH_3 (50 mV/s, pH 11, 0.1 M Na_2SO_4 supporting electrolyte).

respectively [46], indicating the formation of $Ni(OH)_{2(s)}$. The remarkable increase in intensities of these bands that shifted to 475 and 561 cm^{-1} as the potential was raised to +0.4 to +0.8 V, revealed the accumulation of a deeper layer of $NiOOH_{(s)}$, as well as the transformation of α/γ to β/β phases. In the ammonia solution, the additional $\nu_{Ni\text{-}O}$ vibration at 500 cm^{-1} implied that the β phase was highly defective. The oxyhydroxde film mediated electron transfer between the electrode and the nitrogen species over the double layer region, but it practically might take part in the redox of ammonia, which was similar to the oxygen evolution reaction (OER) [47]. For ammonia oxidation, we visualize the flowing steps:

$$Ni^{III}O\text{-}OH + NH_3 \rightarrow Ni^{II}O - NH_{2(ads)} + H_2O \qquad (13)$$

$$2Ni^{II}O\text{-}NH_{2(ads)} \rightarrow 2Ni^{II}O\text{-}N_2H_{4(ads)} \qquad (14)$$

$$2Ni^{II}O\text{-}N_2H_{4(ads)} + 6OH^- \rightarrow 2Ni^{III}O\text{-}OH + N_2\uparrow + 4H_2O + 6e^- \qquad (15)$$

Such protonic defect by donating the first electron of NH_3 to NH_2 (Eq. (13)) is a major step responsible for the crystal distortion during charging/discharging of a Ni electrode. The high degree of disorder demonstrated the appearance of the band at 329 cm^{-1} [48].

Fig. 7a presents XPS spectra of the Ni $2p_{3/2}$ bands and their satellites, which allow the determination of oxidation state on the surface of metallic substrate, for the as-received foam and CV scanned samples. The Ni metal peak at 852.3 eV was within the reported literature value of 852.7±0.4 eV for Ni^0 [49]. Some binding energies (BE) at 853.7 and 855.7 eV ascribed to NiO suggested a partial oxidation of Ni metal upon exposing to the atmosphere. After voltammetry, the intensity of Ni^0 obviously declined and those of $Ni^{II/III}$ in forms of $Ni(OH)_{2(s)}$ and $NiOOH_{(s)}$, at 854.9 eV and 856 eV, respectively, increased [50]. When sweeping the potential between +0.4 and +0.8 V in the presence of 10 mM of NH_3 (Fig. 7b), NiO (853.6 eV) predominated the BE of Ni^{II}. This was in agreement with that the prediction of deprotonic behavior of oxyhydroxide based on Raman analysis (Eq. (15)). At the highest potentials (i.e., +0.6 V to +1.0 V), the absence of surface Ni^0 was resulted entirely from the coating of $Ni(OH)_{2(s)}$. Meanwhile, the mass ratio of $Ni(OH)_{2(s)}$ to $NiOOH_{(s)}$ was reduced by the presence of ammonia,

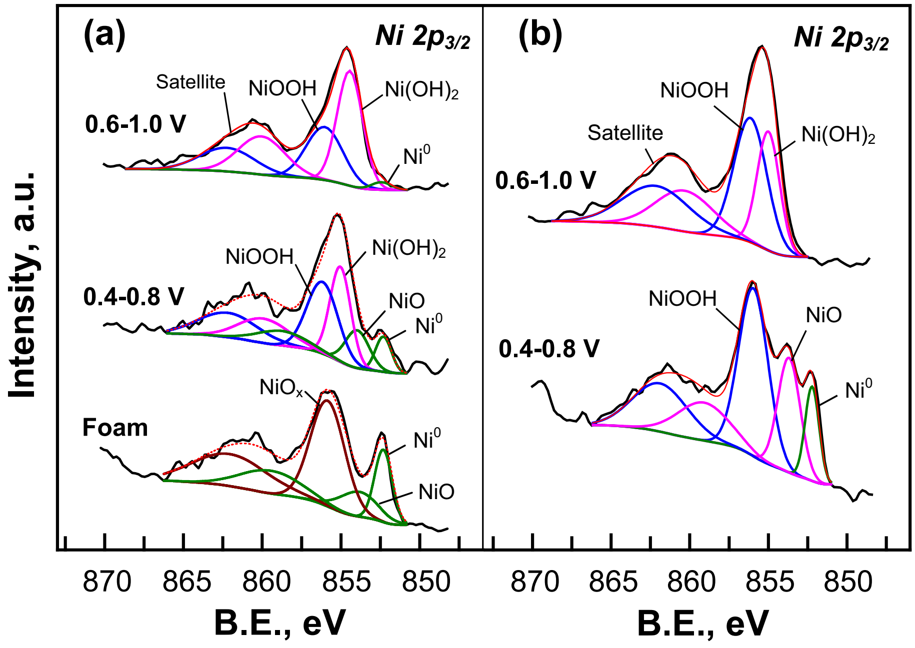

Fig. 7. Ni $2p_{3/2}$ of Ni foam and the CV scanned samples (50 mV/s for 100 cycles, pH 11, 0.1 M Na_2SO_4) (a) without and (b) with 10 mM NH_3.

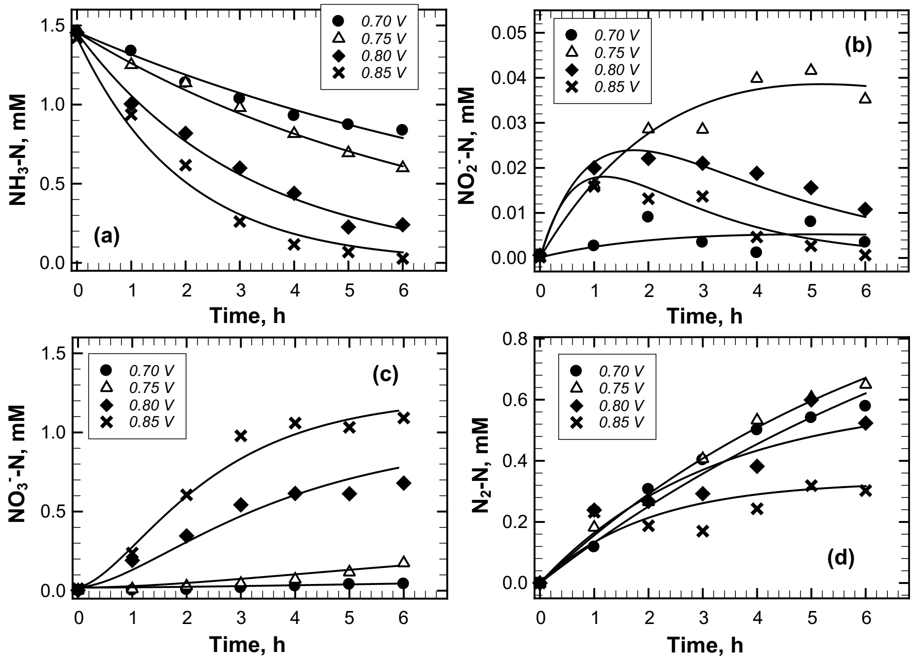

Fig. 8. Concentration changes of nitrogen species (a) NH_3-N, (b) NO_2-N, (c) NO_3-N, and (d) N_2-N at constant potentials of 0.7–0.85 V (vs. Hg/HgO) as a function of reaction time, and those fitted by the proposed kinetics during electrolytic oxidation of ammonia (initial [NH_3-N] = 20 ppm, effective area of working electrode = 40 cm^2, pH 11, 0.1 M Na_2SO_4 electrolyte).

namely NH_3, and its intermediates played a role of discharging the oxyhydroxide.

3.3. Batch experiments of ammonia oxidation on Ni foam electrode

The electrochemical oxidation of ammonia on Ni foam occurred at the potential when $Ni(OH)_{2(s)}$ was oxidized to $NiOOH_{(s)}$, which mediated the $NH_{3(ads)}/NH_{x(ads)}$ redox couple at 0.65–0.7 V (vs. Hg/HgO, Figs. 2b and 3d). The pH was remained at 11 to make sure that NH_3 was the dominant species. During electrolysis, the surface oxidation of nickel consumes OH^- and the ammonia oxidation basically occurs via electrochemical deprotonation, which tends to decrease the solution pH value. Therefore, NaOH addition adjusted the solution pH to 11 after each sampling. To elucidate the effect of working potential on the selectivity of $NH_{x(ads)}$ oxidation to nitrogen gas or nitrogen-oxygen compounds, batch experiments were performed by the oxidation of ammonia at controlled potential. We monitored the temporary concentration of NH_3 and the stable byproducts, namely, NO_2^- and NO_3^-, while that of N_2 was computed via mass-balance, as shown in Fig. 8. Increased the potential from 0.7 to 0.85 V, the removal efficiency of NH_3-N increased from 42 to 98% in 6 h (Fig. 8a). The oxidation of ammonia to the gaseous N_2 took place at 0.7 V, whereas nitrate emerged at potential >0.75 V. Note that the production of nitrite was insignificant (<2.5%), though it was increased during the first hour then decreased as the reaction time was prolonged (Fig. 8b) due to the significant conversion of nitrite to nitrate at 0.8 and 0.85 V (Fig. 8c). The yield of N_2-N reached the highest value of 44.5% at 0.75 V and decreased to 21.3% at 0.85 V (Fig. 8d), as expected by the sequence of electron transfer steps. On the basis of voltammetric observation, the recombination and dehydrogenation of $NH_{x(ads)}$ were brought by two parallel steps, that is, the adsorption of N atom followed by N_2 evolution. At oxidative overpotentials higher than 0.75 V, the formation of oxygen-containing compounds gradually dominated the selectivity to NO_3^-N. We visualize the following scheme as the overall mechanism of ammonia oxidation on the Ni foam electrode:

$$\begin{tikzcd}
 & & & < 0.75V \arrow[r, phantom, "\vdots"] & > 0.75V & \\
NH_{3(aq)} \arrow[r, leftrightarrow, "K_1"] & NH_{3(ads)} \arrow[r, "k_2"] & NH_{2(ads)} \arrow[r, "k_6"] \arrow[d, leftrightarrow, "K_3"] & N_{(ads)} \arrow[r, "k_7"] & NO_2^-{}_{(ads)} \arrow[r, "k_9"] \arrow[d, leftrightarrow, "K_8"] & NO_3^-{}_{(ads)} \arrow[d, leftrightarrow, "K_{10}"] \\
 & & N_2H_{4(ads)} \arrow[d, "k_4"'] & & NO_2^-{}_{(aq)} & NO_3^-{}_{(aq)} \\
 & & N_{2(ads)} \arrow[r, leftrightarrow, "K_5"] & N_{2(g)} & &
\end{tikzcd} \quad (16)$$

Based on reaction scheme of Eq. (16), the concentration variation of ammonia followed the first-order reaction. Moreover, gaseous nitrogen N_2 and nitrogen atom, N, were supposed to form simultaneously from the oxidation of NH_x intermediates. By treating all surface nitrogen species as steady-state species, including θ_{NH3}, θ_{NH2}, θ_N, θ_{N2H4}, θ_{N2}, θ_{NO2}^- and θ_{NO3}^-. (The Supporting Information gives details of the kinetics derivations.), one has:

$$-\frac{dC_{NH3}}{dt} = k_2\theta_{NH3}\theta_{OH} \quad (17)$$

$$\frac{dC_{N2}}{dt} = k_4\theta_{OH}^4\theta_{N2H4} \quad (18)$$

The N atom on surface sites of the working electrode is the primary intermediate further being oxidized to NO_2^- and NO_3^-.

$$\frac{dC_{NO2}}{dt} = k_7\theta_N\theta_{OH}^4 - k_9\theta_{NO2}\theta_{OH}^2 \quad (19)$$

$$\frac{dC_{NO3}}{dt} = k_9\theta_{OH}^2\theta_{NO2} \quad (20)$$

The aqueous nitrogen compounds converted from an initial ammonia dose of $C_{NH3,0}$ including C_{NH3}, C_{N2}, C_{NO2} and C_{NO3}, and the rate of ammonia oxidation was equal to sum of N_2, NO_2^-, and NO_3^-

generation, i.e.,

$$C_{NH3,0} = C_{NH3} + C_{N2} + C_{NO2} + C_{NO3}, \tag{21a}$$

and

$$-r_{NH3} = 2r_{N2} + r_{NO2} + r_{NO3} \tag{21b}$$

Integration of Eqs. (17)–(20) yields the following expressions related to the concentration change of nitrogen species in the solution:

$$C_{NH3} = C_{NH3,0}e^{-k_a t} \tag{22}$$

$$C_{N2} = K_1 C_{NH3,0}\left(1 - e^{-k_a t}\right) \tag{23}$$

$$C_{NO2} = \frac{k_a K_2 (1 - K_1)}{k_b - k_a} C_{NH3,0}\left(e^{-k_a t} - e^{-k_b t}\right) \tag{24}$$

$$C_{NO3} = \frac{(k_b K_3 + k_b K_2 - k_a K_3)(1 - K_1)}{k_b - k_a} C_{NH3,0}\left(1 - e^{-k_a t}\right) - \frac{k_a K_2 (1 - K_1)}{k_b - k_a} C_{NH3,0}\left(1 - e^{-k_b t}\right) \tag{25}$$

where $k_a = \frac{k_1^+ k_2 \theta \theta_{OH}}{k_1^- + k_2 \theta_{OH}}$ and $k_b = \frac{k_8^- k_9 \theta \theta_{OH}^2}{k_9 \theta_{OH}^2 + k_8^+}$, are functions of rate constants and $K_1 = \frac{k_3^+ k_4 \theta_{OH}^3}{k_4 k_3^+ \theta_{OH}^3 + k_3^- k_6 + k_4 k_6 \theta_{OH}^4}$, $K_2 = \frac{k_8^+}{k_9 \theta_{OH}^2 + k_8^+}$, and $K_3 = \frac{k_9 \theta_{OH}^2}{k_9 \theta_{OH}^2 + k_8^+}$ are functions of equilibrium constants ($K_2 + K_3 = 1$) of adsorbed species, including ammonia adsorption and oxidation (k_1^+ & k_2), N_2H_4 combination (k_3^+), N_2 evolution (k_4), NO_2^- desorption/adsorption (k_8^-/k_8^+) and oxidation evolution (k_9), respectively, and can be obtained from fitting the data in Fig. 8. Table 2 lists the rate constants of nitrogen species at various applied potentials. The rate constant of 0.10 h^{-1} for the disappearance of NH_3-N at 0.7 V was increased to 0.51 h^{-1} at 0.85 V, whereas the N_2 dependent combination rate of N_2H_4 was decreased in this potential range. NO_3^- concentration significantly increased by decreasing the desorption rate of and increasing oxidation rate of NO_2^-.

Under controlled potential (0.7–0.85 V), the current efficiency (η_i, %) is defined as the capability of electrode to transfer charges in producing the ith nitrogenous species, i.e.,

$$\eta_i(\%) = \frac{n \times F \times [N_i] \times V}{\int I dt} \tag{26}$$

where $[N_i]$ is the concentration of NO_3^- or NO_2^- or N_2 (M), F is the faradaic constant (96,485 C– eq^{-1}) and V is the reaction volume (L). The electron number "n" involved in the production of NO_3^-, NO_2^- and N_2 was 8, 6 and 3, respectively. The total charge, $Q_{total} = I \times t$, was obtained by integrating the electric current profile (Fig. S6) over reaction time. As summarized in Fig. 9a, interestingly, the charge applied is essentially via NH_3/N_2 over the Ni foam electrode at 0.7 V ($\eta_{N2} = 49\%$). However, the sum of current efficiency of ammonia oxidation ($\eta_{NO3} + \eta_{NO2} + \eta_{N2}$) accounted for less than 25% of the total charge at > 0.7 V. When nickel electrode was charged, accompanying the ammonia oxidation, oxygen evolution reaction was a subsidiary side reaction, which had negative effects on the current efficiency. The oxygen evolution potential (OEP) on pure β-$Ni(OH)_2$ electrode was 547 mV in 1 M KOH solution [41], which was just adjacent to the onset ranges of ammonia oxidization over Ni foam electrode of the present work, although OER could be properly inhibited at pH 11 [51]. On the other hand, direct electro-oxidation of ammonia was influenced by applied potential, in terms of ammonia removal efficiency (NH_{3r}, %) and nitrogen selectivity of conversion (S_N, %), $C_N = [N_2]$ or $[NO_3^-]$ or $[NO_2^-]$ [52].

$$NH_{3r}\ (\%) = \frac{[NH_3]_o - [NH_3]_t}{[NH_3]_o} \times 100 \tag{27}$$

$$S_N\ (\%) = \frac{C_N}{C_{NH3,0} - C_{NH3,t}} \times 100 \tag{28}$$

As shown in Fig. 9b, S_{N2} varied inversely with S_{NO3} and crossed over each other at 0.79 V at which N_2 evolution accounted for half of 80% ammonia removal. A strong selectivity for converting ammonia to nitrogen gas at low overpotential was in agreement with voltammetric result and strongly verified the proposed ammonia oxidation pathway.

Table 2
Oxidation rate constants of different nitrogen products as a function of working potentials.

Rate and equilibrium constant,	Applied potential (vs. Hg/HgO)			
	0.7 V	0.75 V	0.8 V	0.85 V
k_a, h^{-1}	0.1	0.15	0.32	0.51
K_1, a.u.	0.48	0.39	0.19	0.11
k_b, h^{-1}	0.38	0.42	0.5	0.65
K_2, a.u	0.65	0.55	0.09	0.04
K_3, a.u.	0.35	0.45	0.91	0.96

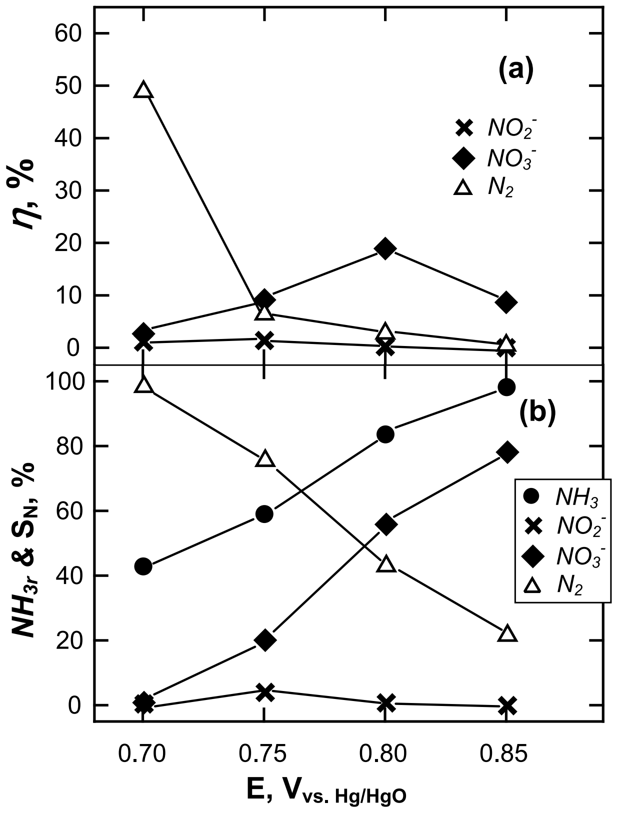

Fig. 9. (a) Current efficiency (η, %) of nickel foam electrode converting ammonia to nitrogen intermediates at various potentials, and (b) NH_3 removal and nitrogen selectivity of conversion (%) at 6 h in Fig. 8.

4. Conclusions

We investigated the electrochemical behavior of ammonia oxidation over a metallic nickel foam electrode in Na_2SO_4 electrolyte (pH 11) by voltammetry and constant potential oxidation experiments. Initial dehydrogenation of NH_3 at potential around the onset of $Ni(OH)_2$/NiOOH redox couple (~0.65 V vs. Hg/HgO) was the key step of direct ammonia oxidation via the specific reduction potential of $Ni(OH)_2$-NiOOH couple. The phase transition between $Ni(OH)_{2(s)}$ and $NiOOH_{(s)}$ was characterized by Raman spectrometry and XPS, which demonstrated clearly the improved oxyhydroxide signal in the presence of NH_3. Based on peak currents from the CV curves in the presence of ammonia at various concentrations, the electron transfer pathway was revealed, i.e., ammonia to gaseous nitrogen occurred at a potential range of 0.7–0.85 V by the oxidation of adsorbed anomia to atomic nitrogen, $N_{(ads)}$, which then dimerized to yield N_2; whereas $N_{(ads)}$ atom was oxidized to oxygen-containing compounds, NO_x, such as NO_2^- and NO_3^- at > 0.75 V. The results of controlled potential experiments showed that the high current efficiency to mineralize ammonia (to non-toxic N_2) occurred at 0.7 V with a rate constant of *ca.* 0.1 h^{-1}. Furthermore, NO_3^--N was the predominant byproduct of the complete oxidation of NH_3-N at higher overpotential.

Acknowledgement

The authors wish to thank The Ministry of Science and Technology – Taiwan, for financial support of this research under Contract No. 104-2218-E-006 -020 -MY3. US, National Science Foundation grant EPSCoR 1632899 provides additional support.

Appendix A. Supplementary data

Supplementary data related to this article can be found at https://doi.org/10.1016/j.electacta.2018.01.045.

References

[1] V. Rosca, M. Duca, M.T. de Groot, M.T.M. Koper, Nitrogen cycle electrocatalysis, Chem. Rev. 109 (2009) 2209–2244.

[2] J.P. Zehr, B.B. Ward, Nitrogen cycle in the ocean: new perspectives on processes and paradigms, Appl. Environ. Microbiol. 68 (2002) 1015–1024.

[3] M. Hauck, F.A. Maalcke-Luesken, M.S.M. Jetten, M.A.J. Huijbregts, Removing nitrogen from wastewater with side stream anammox: what are the trade-offs between environmental impacts? Resour. Conserv. Recycl. 107 (2016) 212–219.

[4] G. Pérez, J. Saiz, R. Ibañez, A.M. Urtiaga, I. Ortiz, Assessment of the formation of inorganic oxidation by-products during the electrocatalytic treatment of ammonium from landfill leachates, Water Res. 46 (2012) 2579–2590.

[5] B. Ma, S. Wang, S. Cao, Y. Miao, F. Jia, R. Du, Y. Peng, Biological nitrogen removal from sewage via anammox: recent advances, Bioresour. Technol. 200 (2016) 981–990.

[6] E. Brillas, C.A. Martínez-Huitle, Decontamination of wastewaters containing synthetic organic dyes by electrochemical methods, an updated review, Appl. Catal. B 166–167 (2015) 603–643.

[7] J.F. Su, I. Ruzybayev, I. Shah, C.P. Huang, The electrochemical reduction of nitrate over micro-architectured metal electrodes with stainless steel scaffold, Appl. Catal. B Environ. 180 (2016) 199–209.

[8] T. Pignet, L.D. Schmidt, Kinetics of NH_3 oxidation on Pt, Rh, and Pd, J. Catal. 40 (1975) 212–225.

[9] N.N. Sazonova, A. Simakov, T.A. Nikoro, G.B. Baranmik, V.F. Lyakhova, V.I. Zhievot, Z.R. Ismgilov, H. Veringa, Selective catalytic oxidation of ammonia to nitrogen, React. Kinet. Catal. Lett. 57 (1995) 71–79.

[10] M. Amblard, R. Burch, B.W.L. Southward, The selective conversion of ammonia to nitrogen on metal oxide catalysts under strongly oxidising conditions, Appl. Catal. B 22 (3) (1999) L159–L166.

[11] L.I. Darvell, K. Heiskanen, J.M. Jones, A.B. Ross, P. Simell, A. Williams, An investigation of alumina-supported catalysts for the selective catalytic oxidation of ammonia in biomass gasification, Catal. Today 81 (4) (2003) 681–692.

[12] L. Gang, B.G. Anderson, J. van Grondelle, R.A. van Santen, NH_3 oxidation to nitrogen and water at low temperatures using supported transition metal catalysts, Catal. Today 61 (1–4) (2000) 179–185.

[13] J.M. Jones, M. Pourkashanian, A. Williams, R.I. Backreedy, L.I. Darvell, P. Simell, K. Heiskanen, P. Kilpinen, The selective oxidation of ammonia over alumina supported catalysts—experiments and modelling, Appl. Catal. B 60 (1–2) (2005) 139–146.

[14] M. Yang, C.Q. Wu, C.B. Zhang, H. He, Selective oxidation of ammonia over copper-silver-based catalysts, Catal. Today 90 (3–4) (2004) 263–267.

[15] R.Q. Long, R.T. Yang, Selective catalytic oxidation of ammonia to nitrogen over Fe_2O_3–TiO_2 prepared with a sol–gel method, J. Catal. 207 (2) (2004) 158–165.

[16] P. Fabrizioli, T. Burgi, A. Baiker, Environmental catalysis on iron oxide–silica aerogels: selective oxidation of NH_3 and reduction of NO by NH_3, J. Catal. 206 (1) (2002) 143–154.

[17] S. Nassos, E.E. Svensson, M. Nilsson, S. Jaras, Microemulsion-prepared Ni catalysts supported on cerium-lanthanum oxide for the selective catalytic oxidation of ammonia in gasified biomass, Appl. Catal. B 64 (1–2) (2006) 96–102.

[18] G. Ramis, M.A. Larrubia, An FT-IR study of the adsorption and oxidation of N-containing compounds over Fe_2O_3/Al_2O_3 SCR catalysts, J. Mol. Catal. A 215 (1–2) (2004) 161–167.

[19] K. Endo, K. Nakamura, Y. Katayama, T. Miura, Pt–Me (Me = Ir, Ru, Ni) binary alloys as an ammonia oxidation anode, Electrochim. Acta 49 (2004) 2503–2509.

[20] C. Zhong, W.B. Hu, Y.F. Cheng, Recent advances in electrocatalysts for electro-oxidation of ammonia, J. Mater. Chem. 1 (2013) 3216–3238.

[21] J. Liu, B. Chen, Y. Kou, Z. Liu, X. Chen, Y. Li, Y. Deng, X. Han, W. Hu, C. Zhong, Pt-Decorated highly porous flower-like Ni particles with high mass activity for ammonia electro-oxidation, J. Mater. Chem. 4 (2016) 11060–11068.

[22] C. Zhang, S.Y. Hwang, Z. Peng, Shape-enhanced ammonia electro-oxidation property of a cubic platinum nanocrystal catalyst prepared by surfactant-free synthesis, J. Mater. Chem. 1 (2013) 14402–14408.

[23] E. Cattaneo, B. Riegel, Chemistry, Electrochemistry, and Electrochemical Applications, Nickel, Elsevier B.V., 2009.

[24] L. Hu, Z. Yu, Z. Hu, Y. Song, F. Zhang, H. Zhu, S. Jiao, Facile synthesis of amorphous $Ni(OH)_2$ for high-performance supercapacitors via electrochemical assembly in a reverse micelle, Electrochim. Acta 174 (2015) 181–273.

[25] A. Kapałka, A. Cally, S. Neodo, C. Comninellis, M. Wächter, K.M. Udert, Electrochemical behavior of ammonia at Ni/$Ni(OH)_2$ electrode, Electrochem. Commun. 12 (2010) 18–21.

[26] C. Tang, Z. Pu, Q. Liu, A.M. Asiri, Y. Luo, X. Sun, Ni_3S_2 nanosheets array supported on Ni foam: a novel efficient three-dimensional hydrogen-evolving electrocatalyst in both neutral and basic solutions, Int. J. Hydrogen Energy 40 (2015) 4727–4732.

[27] C. Tang, L. Xie, K. Wang, G. Du, A.M. Asiri, Y. Luo, X. Sun, A Ni_2P nanosheet array integrated on 3D Ni foam: an efficient, robust and reusable monolithic catalyst for the hydrolytic dehydrogenation of ammonia borane toward on-demand hydrogen generation, J. Mater. Chem. 4 (2016) 12407–12410.

[28] X. Zhou, Z. Xia, Z. Zhang, Y. Ma, Y. Qu, One-step synthesis of multi-walled carbon nanotubes/ultra-thin $Ni(OH)_2$ nanoplate composite as efficient catalysts for water oxidation, J. Mater. Chem. 2 (2014) 11799–11806.

[29] B.M. Stewart, Effect of temperature on the formation of indophenol blue in a spectrophotometric method for the determination of ammonia, Water Res. 19 (1985) 1443–1445.

[30] B.S. Gentle, P.S. Ellis, M.R. Grace, I.D. McKelvie, Flow analysis methods for the direct ultra-violet spectrophotometric measurement of nitrate and total nitrogen in freshwaters, Anal. Chim. Acta 704 (2011) 116–122.

[31] W. Su, L. Zhang, Y. Tao, G. Zhan, D. Li, D. Li, Sulfate reduction with electrons directly derived from electrodes in bioelectrochemical systems, Electrochem. Commun. 22 (2012) 37–40.

[32] D. Kartikaningsih, Y.H. Huang, Y.J. Shih, Electro-oxidation and characterization of nickel foam electrode for removing boron, Chemosphere 166 (2017) 184–191.

[33] S. Xu, Y. Zhu, D. Xiong, W. Zhang, L. Wang, P. Yang, P.K. Chu, Electrochemical investigation of the corrosion properties of three-dimensional nickel electrodes on silicon microchannel plates, Corrosion Sci. 100 (2015) 113–120.

[34] M. Wehrens-Dijksma, P.H.L. Notten, Electrochemical Quartz Microbalance characterization of $Ni(OH)_2$-based thin film electrodes, Electrochim. Acta 51 (2006) 3609–3621.

[35] M.E.G. Lyons, M.P. Brandon, A comparative study of the oxygen evolution reaction on oxidised nickel, cobalt and iron electrodes in base, J. Electroanal. Chem. 641 (2010) 119–130.

[36] J. van Drunen, B. Kinkead, M.C.P. Wang, E. Sourty, B.D. Gates, G. Jerkiewicz, Comprehensive structural, surface-chemical and electrochemical characterization of nickel-based metallic foams, Appl. Mater. Interfaces 5 (2013) 6712–6722.

[37] Q. Zhou, M. Cui, K. Tao, Y. Yanga, X. Liu, L. Kang, High areal capacitance three-dimensional Ni@$Ni(OH)_2$ foams via in situ oxidizing Ni foams in mild aqueous solution, Appl. Surf. Sci. 365 (2016) 125–130.

[38] K.S. Lee, M.S. Park, J.D. Kim, Nitrogen doped activated carbon with nickel oxide for high specific capacitance as supercapacitor electrodes, Colloids Surf., A 533 (2017) 323–329.

[39] Q.S. Song, C.H. Chiu, S.L.I. Chan, Performance improvement of pasted nickel electrodes with an addition of ball-milled nickel hydroxide powder, Electrochim. Acta 51 (2006) 6548–6555.

[40] Y.W. Li, J.H. Yao, C.J. Liu, W.M. Zhao, W.X. Deng, S.K. Zhong, Effect of interlayer anions on the electrochemical performance of Al-substituted α-type nickel hydroxide electrodes, Int. J. Hydrogen Energy 35 (2010) 2539–2545.

[41] B. Shruthi, B.J. Madhu, V.B. Raju, Influence of TiO_2 on the electrochemical performance of pasted type β-nickel hydroxide electrode in alkaline electrolyte, J. Energy Chem. 25 (2016) 41–48.

[42] G. Bontempelli, R. Toniolo, Measurement Methods | Electrochemical: Linear Sweep and Cyclic Voltammetry-reference Module in Chemistry, Molecular Sciences and Chemical Engineering, Encyclopedia of Electrochemical Power Sources, Elsevier B.V., 2009, pp. 643–654.

[43] Q. Chen, D. Cai, H. Zhan, Interconnected Ni-Co sulfide nanosheet arrays grown on nickel foam as binder-free electrodes for supercapacitors with high areal capacitance, J. Alloy. Comp. 721 (2017) 205–212.

[44] N.J. Bunce, D. Bejan, Mechanism of electrochemical oxidation of ammonia, Electrochim. Acta 56 (2011) 8085–8093.

[45] F.J. Vidal-Iglesias, J. Solla-Gullón, J.M. Feliu, H. Baltruschat, A. Aldaz, DEMS study of ammonia oxidation on platinum basal planes, J. Electroanal. Chem. 588 (2006) 331–338.

[46] B.D. Yeo, A.T. Bell, In situ Raman study of nickel oxide and gold-supported nickel oxide catalysts for the electrochemical evolution of oxygen, J. Phys. Chem. C 116 (2012) 8394–8400.

[47] K. Juodkazis, J. Juodkazytė, R. Vilkauskaitė, V. Jasulaitienė, Nickel surface anodic oxidation and electrocatalysis of oxygen evolution, J. Solid State Electrochem. 12 (2008) 1469–1479.

[48] S. Deabate, F. Fourgeot, F. Henn, J. Power Sources 87 (2000) 125–136.

[49] S. Deabate, F. Fourgeot, F. Henn, X-ray diffraction and micro-Raman spectroscopy analysis of new nickel hydroxide obtained by electrodialysis, J Power Source 87 (2000) 125–136.

[50] M.C. Biesinger, B.P. Payne, L.W.M. Lau, A. Gerson, R. St C. Smart, X-ray photoelectron spectroscopic chemical state quantification of mixed nickel metal, oxide and hydroxide systems, Surf. Interface Anal. 41 (2009) 324–332.

[51] L. Giordano, B. Han, M. Risch, W.T. Hong, R.R. Rao, K.A. Stoerzinger, Y. Shao-Horn, pH dependence of OER activity of oxides: current and future perspectives, Catal. Today 262 (2016) 2–10.

[52] G. Moussavi, M. Mahdavianpour, The selective direct oxidation of ammonium in the contaminated water to nitrogen gas using the chemical-less VUV photochemical continuous-flow reactor, Chem. Eng. J. 295 (2016) 57–63.